

Numerical Integration of Barotropic Vorticity Equation with Spectral Method

傅豪 Hao Fu

2017.2.20 @ IAP

Abstract

A barotropic vorticity equation (BVE) model is established with spectral method in Fortran 90 code, MPI parallelized. For Cartesian coordinate, decaying 2D turbulence on f plane and beta plane is simulated. Some analysis on energy spectrum and flow field are presented, and some personal understanding has been added to illustrate the theory.

1. Introduction

The atmosphere and ocean consists of various scales of motion, and could be depicted by a hierarchy of models. “To start from 3D GCM or 2D BVE, that is a question”. Here, I adopt the later one. The large scale dynamics of mid-latitude atmosphere and ocean is quasi-hydrostatic, with large aspect ratio. Therefore, 2D (one layer) shallow water equations is adequate to depict large scale dynamics, with baroclinic and convective processes parameterized in the forcing term. In the middle and high latitude, the relatively strong Coriolis force further constrains the flow to be quasi-geostrophic, and therefore the barotropic QG equation is obtained as a first order result of small parameter expansion. Further constraining the flow to be non-divergent leads to the barotropic vorticity equation, which is in fact two dimensional incompressible N-S equations.

$$\frac{\partial}{\partial t} \nabla^2 q + J(\psi, \nabla^2 q) = F, \text{ where } q = \nabla^2 \psi + f \quad (1.1)$$

The linear advection term gives rise to interactions between different scales of motion (including Rossby wave triad interaction), and makes the flow turbulent and chaotic. Therefore, in a zero-order sense, the atmosphere and ocean could be viewed as forced two-dimensional turbulence, with forcing coming from baroclinic instability, wave breaking or Ekman pumping etc. When beta effect is taken into account, the upscaling ends up with Rossby wave and zonal jets.

2. Model description

Spectral method is among the family of Galerkin method which involves projecting the variable and the equation to a new space and use maximum value principle (usually in a least square sense) to look for the projection coefficients and its prognostic equation (Zhang et al., 1991).

$$J(\hat{\psi}) = \int_D (\hat{\psi} - \psi)^2 dx \quad (2.0.1)$$

2.1 The nature of spectral method

Spectral method is distinct from grid points method in that it offers a perspective on “simulating waves”. For linear problems, so long as the transform is accurate, the only error comes from time discretization. Even with time error, for linear fully-discretized advection

equation, the phase speed is still correct. The spectral method's order of accuracy depends on the smoothness of the solution (while finite difference method does not). It boasts extraordinary high accuracy in smooth region, and suffers from numerical oscillation in unsmooth region (Durran, 2009).

This may not be a problem for BVE, as discontinuity never evolves in 2D turbulence (Durran, 2009) free from forcing, which is due to the upscale cascading of kinetic energy. Maybe the elliptic nature of the equation also prevents discontinuity from evolving, for there is no real characteristic line. In fact, it is the approaching of characteristic lines that cause shock wave. In the inviscid limit, however, if the initial condition is not derivative, an infinite thin vorticity inviscid shear layer for example, then the flow evolution could be very complicated. The well-posedness of the problem is in doubt and should be regularized in numerical simulation [vortex]. When the fluid is viscous, viscosity can smooth the flow field.

2.1 spectral transform and its inversion

Firstly, we expand the initial field with a complete set of orthogonal functions. Here we limit our discussion to finite domain size, with Dirichlet, Neumann or periodic boundary condition. The function space is in fact the solution space of Sturm-Liouville eigenvalue problem. This is an infinite-dimension Hilbert space, with well-defined norm, inner product, and is complete. In order to record the projection coefficient in a computer, we usually use its subspace with finite dimension. This is done by truncating the infinite series to a finite one.

2.1.1 Cartesian geometry

Fourier series is usually used in Cartesian geometry, because triangular function is the eigen-function of Laplace equation in Cartesian geometry, and is especially convenient for uniform grid system. For non-uniform grid, Laguerre polynomials and Legendre polynomials can also be used[].

The forward transform reads:

$$\psi_{m,n} = \frac{1}{L_x L_y} \int_{-L_x/2}^{L_x/2} \int_{-L_y/2}^{L_y/2} \psi(x,y) \exp[-i(\frac{m\pi}{L_x}x + \frac{n\pi}{L_y}y)] dx dy, (x,y) \in [-\frac{L_x}{2}, \frac{L_x}{2}] \otimes [-\frac{L_y}{2}, \frac{L_y}{2}]$$

(2.1.1.1)

And in a case usually used for 2D turbulence simulation:

$$\psi_{m,n} = \frac{1}{(2\pi)^2} \int_0^{2\pi} \int_0^{2\pi} \psi(x,y) \exp[-i(mx + ny)] dx dy, (x,y) \in [0, 2\pi] \otimes [0, 2\pi]$$

(2.1.1.2)

This case will be used in the following part. It's obvious that :

$$\psi_{m,n} = \psi_{-m,-n} \quad (2.1.1.3)$$

We may use rectangular formula to integrate it, and leads to the so-called discrete Fourier transform (DFT):

$$\psi_{m,n} = \frac{1}{XY} \sum_{i_x=0}^{X-1} \sum_{i_y=0}^{Y-1} \psi(x,y) \exp[-i(m \frac{2\pi i_x}{X} \Delta x + n \frac{2\pi i_y}{Y} \Delta y)], m \in [-M, M], n \in [-N, N]$$

(2.1.1.4)

With Xsize equivalent grid points, $\psi(x,y)\exp[-i(mi_x\Delta x + ni_y\Delta y)]$ should contain less than (Xsize) $\exp(-i i_x\Delta x)$ components to be computed accurately. It indicates a wavenumber truncation principle:

$$X \leq 2M + 1 \quad (2.1.1.5)$$

Otherwise, excess information on the equivalent grid points will be aliased into other representable components, causing aliasing error. It occurs whenever there is too many waves to represent with finite wavenumbers, and is essentially one kind of “wavenumber truncation error”. Aliasing error have two types, with one type appearing when we are preparing for initial value with a series of oscillatory sample points (“initial aliasing error”), and the other type when calculating nonlinear terms. The error caused by infinite grid points is called “spatial truncation error”, and the fact that only limited wavenumber could be transformed to spectral space causes “wavenumber truncation error”.

The Fourier series converge quite fast, with the m^{th} wave’s amplitude estimated to be:

$$|a_m| \leq \frac{c}{|m|^p} \quad (2.1.1.6)$$

Where c is a constant, and p means the function has up to $(n - 1)^{th}$ order of derivatives (Zhang et al., 1991). This is easily proved by integration by parts of the a_m ’s expression. The smoother the function, the faster it converges.

The inverse (discrete) transform is straightforward and does not add any truncation error:

$$\psi(x, y, t) = \sum_{-\infty}^{+\infty} \sum_{-\infty}^{+\infty} \psi_{m,n}(t) \exp(imx) \exp(iny) \approx \sum_{-M}^M \sum_{-N}^N \psi_{m,n}(t) \exp[i(mx + ny)] \quad (9)$$

In the algorithm, the 2D and 3D DFT can be separated into two sequential 1D DFT operations. For 2D and 3D, however, the truncation scheme is less obvious. Most researchers seem to truncate with a rectangular (or square) domain on the (m,n) space, is that isotropic and optimal?

Both DFT and inverse DFT(IDFT) involves $O(Msize * Xsize, Nsize * Ysize) \approx O(Xsize^2)$ complex summation operations, and is computationally inhibited for large Xsize. Two techniques are introduced to fasten the speed: FFT and MPI parallel computing which is described in the appendix.

For homogeneous Dirichlet boundary condition $u|_{\partial\Omega} = 0$, “odd prolongation” is done, while for homogeneous Neumann condition $\frac{\partial u}{\partial n}|_{\partial\Omega} = 0$, “even prolongation” is done. The expansion function is no longer $\exp(imx)$, but $\cos(mx)$ and $\sin(mx)$ instead.

The choice of eigen-functions is not limited to triangular function. like Chebyshev-tau polynomials also apply to Cartesian geometry,

2.1.2 Spherical geometry

spherical harmonic function composes the solution space of spherical harmonic equation.

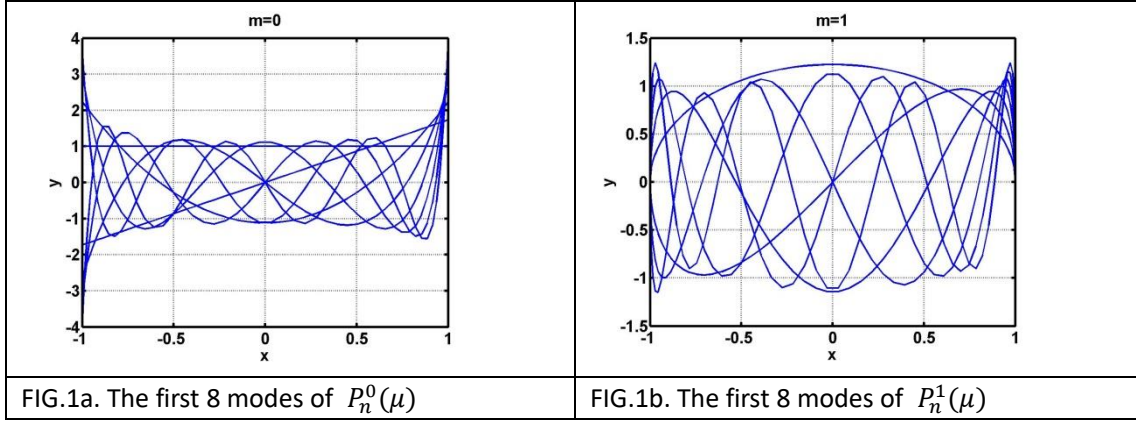
$$Y_n^m(\lambda, \mu) = P_n^m(\mu) \exp(im\lambda) \quad , \quad \mu = \sin\varphi \quad , \quad m=0,1,2,\dots \quad n=0,1,2 \quad \dots, \quad |m| \leq n \quad (2.1.2.1)$$

$$\Psi(\lambda, \mu) = \sum_{n=|m|}^{+\infty} \sum_{m=-\infty}^{+\infty} Z_{mn} Y_n^m(\lambda, \mu)$$

$$Z_{mn} = \frac{1}{4\pi} \int_0^{2\pi} \int_{-1}^1 \psi(\lambda, \mu) (Y_n^m)^* d\mu d\lambda$$

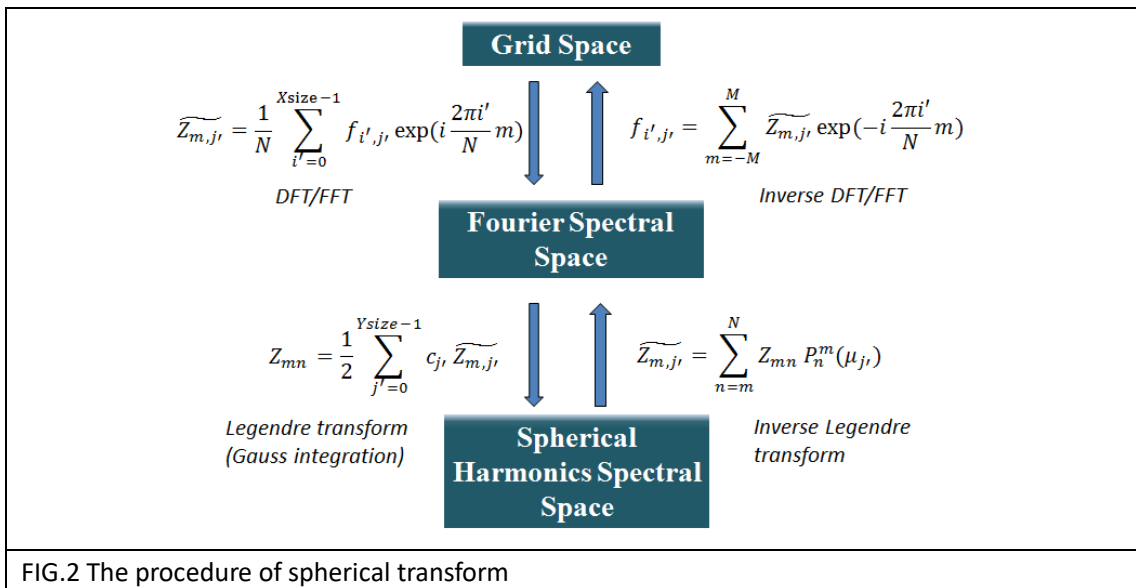
The associated Legendre function $P_n^m(\mu)$ has the follow properties:

- (1) $P_n^m(\mu) = P_n^{-m}(\mu)$, and this leads to $[Y_n^m(\mu)]^* = Y_n^{-m}(\mu)$
- (2) $P_n^m(-\mu) = (-1)^{n-|m|} P_n^m(\mu)$, this is useful for making semi-sphere model.



The spherical harmonic transform consists of one Fourier transform and one Legendre transform. The Legendre transform $Z_{mn} = \frac{1}{2} \int_{-1}^1 f(\mu) d\mu$ is discretized as a Gaussian-Legendre integration, with the quadrature points chosen as the zero point of $P_n^0(\mu)$. This has a $(2Y - 1)^{th}$ order of accuracy.

Using Bessel-Parseval identity, one can prove that $Z_{mn} \sim O(\frac{1}{n^{2p}})$ for sufficiently large n, where p is a measure of differentiability, thus $Y_n^m(\lambda, \mu)$ also converges very fast for a smooth $\psi(\lambda, \mu)$.



2.2 spectral equation

After expanding the PDE with the same set of functions, and obtains a complex-value ODE

for the projection coefficients. For periodic or confined domain, this procedure is similar to the “Fourier series method” in solving inhomogeneous linear PDE (Liang). With ODE and its initial value, time derivative still need to be discretized (usually with finite difference) to do time stepping.

2.2.1 Cartesian geometry

The BVE in conservative form reads:

$$\frac{\partial}{\partial t} \nabla^2 \psi - \frac{\partial}{\partial x} \left(\frac{\partial \psi}{\partial y} \nabla^2 \psi \right) + \frac{\partial}{\partial y} \left(\frac{\partial \psi}{\partial x} \nabla^2 \psi \right) + \beta \frac{\partial \psi}{\partial x} = \nu \nabla^4 \psi - \frac{1}{\tau_{dis}} \nabla^2 \psi \quad (2.2.1.1)$$

It's happy that all the derivative operators' have their eigen-functions in Fourier space.

$$\mathcal{L}u = \lambda u : \quad \frac{\partial}{\partial x} = im, \quad \frac{\partial}{\partial y} = in, \quad \nabla^2 = -(m^2 + n^2) \quad (2.2.1.2)$$

We get the spectrum ODE:

$$-(m^2 + n^2) \frac{dZ_{mn}}{dt} = -\mathcal{F} \left(\frac{\partial}{\partial x} \left(\frac{\partial \psi}{\partial y} \nabla^2 \psi \right) + \frac{\partial}{\partial y} \left(\frac{\partial \psi}{\partial x} \nabla^2 \psi \right) \right) - im\beta Z_{mn} + \nu [-(m^2 + n^2)]^2 - \frac{1}{\tau_{dis}} [-(m^2 + n^2)], \quad \text{where } \mathcal{F}(u) = \frac{1}{4\pi} \int_0^{2\pi} \int_{-1}^1 u(Y_n^m) * d\mu d\lambda \quad (2.2.1.3)$$

The nonlinear term $\mathcal{F}(u)$ needs a special treatment, for it involves interaction between different waves. One way is to project it directly to spectral space, and obtaining a huge coupled set of ODE, called “Silberman direct method”. This requires to store the “interactive coefficients” preliminarily in the computer and is quite complicated, even though accurate. An alternative is the so called “transform method” introduced by Orszag (Durrant, 2009). The products of two variables are calculated in grid space, and transform back to spectral space. For example, when we want to calculate $\mathcal{F}(C)$ with $C = A \cdot B$,

$$\mathcal{F}(C) = \mathcal{F}(A \cdot B) = \mathcal{F}(\mathcal{F}^{-1}(A) \cdot \mathcal{F}^{-1}(B)), \quad (2.2.1.4)$$

The only thing to concern is aliasing error produced by the product. Similar to the proof of (), we get the de-aliasing condition:

$$X \leq 3M + 1, \quad Y \leq 3N + 1 \quad (2.2.1.5)$$

2.2.2 Spherical geometry:

BVE in spherical geometry reads:

$$\frac{\partial}{\partial t} \nabla^2 \psi = -\frac{\partial}{\partial \lambda} \left(\frac{U \zeta_a}{a(1-\mu^2)} \right) - \frac{\partial}{\partial \mu} (V \zeta_a) + \nu \nabla^4 \psi - \frac{1}{\tau_{dis}} \nabla^2 \psi \quad (2.2.2.1)$$

$$U = u \cos \varphi, \quad V = v \cos \varphi \quad \zeta_a = \nabla^2 \psi + f, \quad \text{where } a \text{ is Earth's radius}$$

It's impossible to define the velocity vector at pole points with spherical coordinate, so we arbitrarily set the velocity there to be zero by introducing pseudo-velocity U and V. This may be adequate when the flow is quasi-axisymmetric. In real spectral GCM, pole points are usually

treated by rotating the coordinate.

As for the derivatives, we have:

$$\frac{\partial}{\partial \lambda} = im \quad , \quad \nabla^2 = -\frac{n(n+1)}{a^2} \quad (2.2.2.2)$$

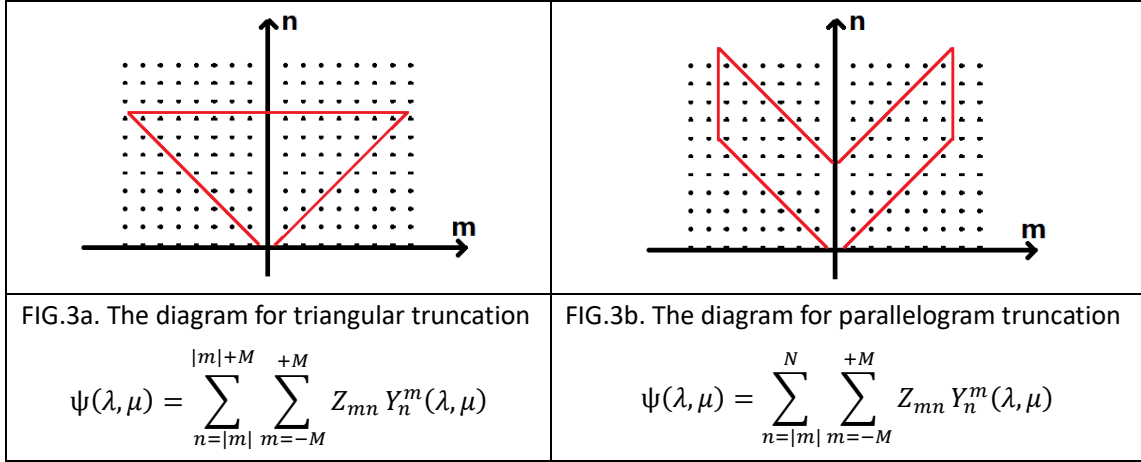
Y_n^m is unfortunately not the eigen-function of $\partial/\partial\mu$, but we can use integration by parts to transfer $\partial/\partial\mu$ onto P_n^m , similar to the derivative of test function in finite-element method. The advantage of expressing the equation in conservative form just lies here. For example:

$$\begin{aligned} \int_{-1}^1 \int_0^{2\pi} \frac{\partial(V\zeta_a)}{\partial\mu} P_n^m(\mu) \exp(im\lambda) d\lambda d\mu &= \int_0^{2\pi} (V\zeta_a)|_{\mu=-1,1} P_n^m \exp(im\lambda) d\lambda d\mu \\ &- \int_{-1}^1 \int_0^{2\pi} V\zeta_a \frac{dP_n^m}{d\mu} \exp(im\lambda) d\lambda d\mu \end{aligned} \quad (2.2.2.3)$$

The spectrum equation is readily obtained:

$$-\frac{n(n+1)}{a^2} \frac{dZ_{mn}}{dt} = \mathcal{F} \left(-\frac{\partial}{\partial \lambda} \left(\frac{U\zeta_a}{a(1-\mu^2)} \right) - \frac{\partial}{\partial \mu} (V\zeta_a) \right) + \nu \left[-\frac{n(n+1)}{a^2} \right]^2 - \frac{1}{\tau_{dis}} \left[-\frac{n(n+1)}{a^2} \right] \quad (2.2.2.4)$$

There are mainly two types of truncation schemes: triangular and parallelogram. The former is rotationally-invariant, good for pole points treatment. They also have different spatial resolution distribution, and detailed analysis can be found in (Zhang et al., 1991).



We choose triangular truncation. The de-aliasing condition is obtained by considering the accuracy of DFT and Legendre transform:

$$X \leq 3M + 1, \quad Y \leq (3M + 1)/2 \quad (2.2.2.5)$$

2.3 Time stepping scheme

The viscous vorticity equation is a convection-diffusion equation. Following [], we adopt 3rd order Runge-Kutta TVD (total deviation diminishing) scheme

$$\begin{aligned} \psi_1 &= \psi^n + \Delta t L(\omega_0) \\ \psi_2 &= 3/4\psi^n + 1/4[\psi_1 + \Delta t L(\psi_1)] \\ \psi^{n+1} &= 1/3\psi^n + 2/3[\psi_2 + \Delta t L(\psi_2)] \end{aligned} \quad (2.3.1)$$

TVD is define as :

$$TV = \sum_{i=0}^{X-1} |\psi_i - \psi_{i-1}|, \quad TV^{n+1} \leq TV^n \quad (2.3.2)$$

This scheme is actually a convex combination of Euler forward. These coefficients guarantee that so long as Euler forward is TVD (with certain spatial discretization scheme), this high order scheme is TVD too.

We use 1D advection–diffusion advection to analyze the linear stability condition, assuming spatial derivatives are accurate, and focus on time stepping scheme. Substituting a normal mode into the PDE, $\psi = \Psi \exp(ikx)$,

$$\frac{\partial \psi}{\partial t} = -c \frac{\partial \psi}{\partial x} + \nu \frac{\partial^2 \psi}{\partial x^2} \quad (2.3.3)$$

We get:

$$\begin{aligned} \frac{d\Psi}{dt} &\approx \lambda + i\omega = \left[-\frac{k^2}{Re} + i(-kc) \right] \Psi = B\Psi \\ \Psi_1 &= (1 + \Delta t B) \\ \Psi_2 &= \frac{3}{4} + \frac{1}{4} \Psi_1 (1 + \Delta t B) \end{aligned} \quad (2.3.4)$$

$$\begin{aligned} \text{We get } A(\lambda, \omega) &= \frac{\Psi_{n+1}}{\Psi_n} = \frac{1}{3} + \frac{2}{3} \Psi_2 (1 + \Delta t B) = \frac{1}{3} + \frac{2}{3} (1 + \Delta t B) \left[\frac{3}{4} + \frac{1}{4} (1 + \Delta t B)^2 \right] \\ (2.3.5) \end{aligned}$$

The stability region is plotted in FIG.4

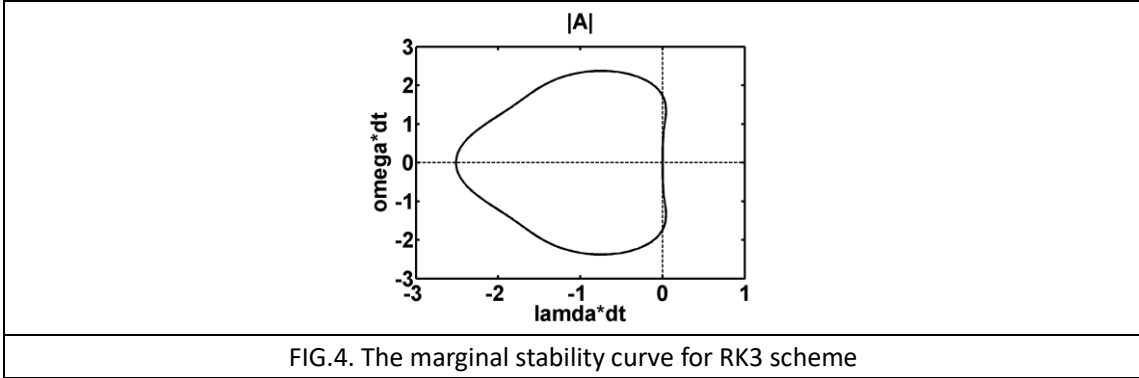


FIG.4. The marginal stability curve for RK3 scheme

Stability requires $\lambda \Delta t > -2.515$, that is $\nu k^2 \Delta t < 2.515$; with $\omega_{max} \approx 2.333$, that is $kc \Delta t < 2.333$.

We now apply the result to 1D BVE. With the same normal mode, and $\nabla^2 = -k^2$.

$$\frac{\partial \nabla^2 \psi}{\partial t} = -c \frac{\partial \nabla^2 \psi}{\partial x} - \beta \frac{\partial \psi}{\partial x} + \nu \frac{\partial^2}{\partial x^2} (\nabla^2 \psi) \quad (2.3.6)$$

$$\text{We have: } (-k^2) \frac{d\Psi}{dt} = -c(ik)^3 \Psi - ik\beta \Psi + \nu(ik)^3 \Psi \quad (2.3.7)$$

$$\frac{d\Psi}{dt} \approx \lambda + i\omega = \left[-\frac{k^2}{Re} + i \left(-kc + \frac{\beta}{k} \right) \right] \Psi = B\Psi \quad (2.3.8)$$

thus, the stability condition reads,

$$\Delta t \leq \min \left(\frac{2.515}{\nu k^2}, \left| \frac{2.333}{kc_p} \right| \right) \leq \min \left(\frac{2.515}{\nu M^2}, \frac{2.333}{M(|c| + \beta)} \right) \quad (2.3.9)$$

where $c_p = c - \frac{\beta}{k^2}$ is Rossby wave phase speed and substituted c in (). The longest Rossby wave is also the most unstable wave, with $k = 1$.

2.4 conservation property

The inviscid BVE conserves total kinetic energy (E) and total enstrophy (V). For spectrum method, with Bessel-Parseval identity, such quantities are easily calculated with the summation of spectrum coefficients. On Cartesian geometry, the expression is:

$$E = \iint \frac{1}{2} \psi \nabla^2 \psi dS = \iint \frac{1}{2} (u^2 + v^2) dS = \iint \frac{1}{2} u^2 dS + \iint \frac{1}{2} v^2 dS$$

$$= \frac{1}{2} \sum_{m=-M}^M \sum_{n=-N}^N |imZ_{mn}|^2 + |inZ_{mn}|^2 = \frac{1}{2} \sum_{m=-M}^M \sum_{n=-N}^N (m^2 + n^2) |Z_{mn}|^2 \quad (2.4.1)$$

$$V = \iint \frac{1}{2} |\nabla^2 \psi|^2 dS = \frac{1}{2} \sum_{m=-M}^M \sum_{n=-N}^N |(m^2 + n^2) Z_{mn}|^2 = \frac{1}{2} \sum_{m=-M}^M \sum_{n=-N}^N (m^2 + n^2)^2 |Z_{mn}|^2$$

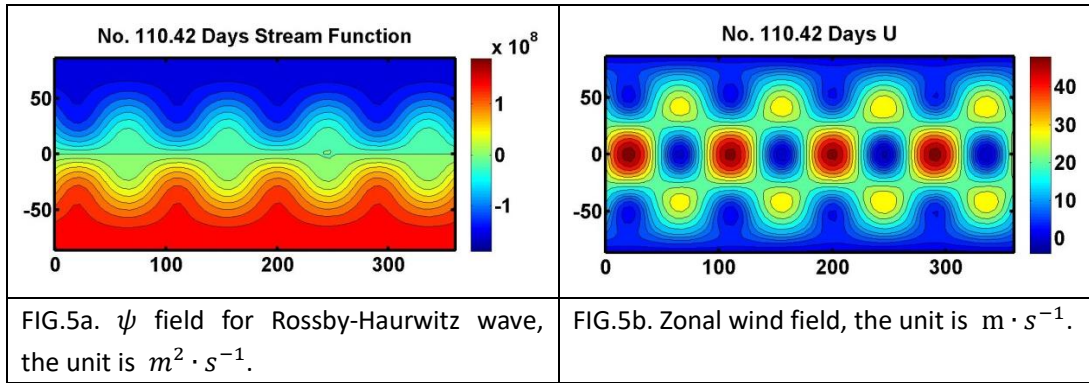
(2.4.2)

On spherical geometry, I haven't been able derive the expression of E, and only V is shown here:

$$V = \iint \frac{1}{2} |\nabla^2 \psi|^2 dS = \frac{1}{2} \sum_{m=-M}^M \sum_{n=-N}^N \left| \frac{n(n+1)}{a^2} Z_{mn} \right|^2 = \frac{1}{2} \sum_{m=-M}^M \sum_{n=-N}^N \left[\frac{n(n+1)}{a^2} \right]^2 |Z_{mn}|^2 \quad (2.4.3)$$

3. Rossby-Haurwitz wave test

Rossby-Haurwitz wave (RH wave) is the exact solution of fully nonlinear BVE on the sphere. The theory predicts a travelling wave solution, with a period of 60.66 days. In our simulation, the period is about 60 days, and the wave broke down after about 110 days.



4. 2D turbulence without beta effect

Technically speaking, 2D turbulence is only an approximation to real 3D turbulence and does not exist in nature. When the a vertical column of fluid moves synchronously, that is when $\frac{\partial}{\partial z} \approx 0$, the fluid is quasi-2D, with no vertical advection, diffusion and vortex tube stretching and

tilting. Various physical setting leads to the quasi-2D phenomenon --- a geometry with large aspect ratio: $\Gamma = L/H$, a strong background rotation (Taylor-Proudman theorem), or a strong stratification. The motion of soap film is quasi-2D due to its small Γ , and is usually used in laboratory study of 2D turbulence. Large scale atmospheric and oceanic motion is quasi-2D due

to small Γ , small Ro , and stratification, with baroclinic effects parameterized in eddy forcing term []].

The motivation of this study is reproducing 2D turbulence, and the role of beta effect. I use non-dimensionalized BVE, with $u = Uu'$, $x = Lx'$, $Re = UL/\nu$, $\beta^* = \beta L^2/U$ called Rossby parameter which depicts the relative strength of β effect.

$$\frac{\partial}{\partial t} \nabla^2 \psi + J(\psi, \nabla^2 \psi) = \frac{1}{Re} \nabla^4 \psi - \beta^* v \quad (4.0.1)$$

These are free decaying simulations, and I shall change Re and β^* for different simulations.

4.1 Prediction of energy cascade in 2D turbulence

Turbulence involves a variety of scale, and I suppose the transfer of a quantity in wavenumber space could be called "cascade". Cascade is caused by nonlinear advection term (rather than diffusion). There are three nonlinear processes in 3D turbulence: vorticity elongation by advection, vortex stretching and tilting. Consecutive vortex stretching leads to vortex contraction and strengthening until it reaches Kolmogorov length scale and dissipates [first course], causing enstrophy downscale cascade in 3D turbulence. Only vorticity elongation occurs in 2D turbulence. This leads to a dramatic distinction from its three-dimensional counterpart --- both energy and enstrophy is conserved without forcing, and they have implications on energy and enstrophy cascade direction.

Vorticity elongation produces vortex filamentation in 2D (and I think 3D as well). The elongation may root in the advection caused by the straining part of $\nabla \vec{u}$, with the contribution from deformation $S_1 = \frac{\partial u}{\partial x} - \frac{\partial v}{\partial y}$ and shearing $S_2 = \frac{\partial v}{\partial x} + \frac{\partial u}{\partial y}$, (Wang et al., 2010). While vorticity stretching can increase vorticity magnitude due to angular momentum conservation, straining can't change, and the area of each closed vorticity contour line is conserved in inviscid straining field. As vorticity is a Lagrangian quantity, elongation makes a vortex more asymmetric, with a larger vorticity length scale in elongation direction and a shorter one in the other. The 2D (full wavenumber) spectrum must broaden. With this, there is a quantitative theory. Suppose that dissipation is weak (this maybe valid for an initial stage with large wavelength energy injection, far larger than dissipation scale). Defining central wavenumber k_E (the first order origin moment) and wavenumber bandwidth Δk_E , with $E(k)$ denoting the 2D energy spectrum (with full wavenumber)

$$k_E = \int_0^\infty k E(k) dk / \int_0^\infty E(k) dk \quad (4.1.1)$$

$$\Delta k_E = \int_0^\infty (k - k_E)^2 E(k) dk / \int_0^\infty E(k) dk \quad (4.1.2)$$

With the constraint $\frac{dE}{dt} = \frac{d}{dt} \int_0^\infty E(k) dk = 0$, $\frac{dV}{dt} = \frac{d}{dt} \int_0^\infty k^2 E(k) dk = 0$, we can prove that,

when $\frac{d\Delta k_E}{dt} > 0$ (the spectrum broadens), $\frac{dk_E}{dt} > 0$ (the kinetic energy's central wavenumber goes upscale) (McWilliams, 2006). The decreasing tendency of central enstrophy wavenumber is proved in a similar away.

In addition,

Here I have two questions:

- (1) It seems paradoxical that the second order origin moment k_M^2 is constant, as is denoted in many Chinese textbooks as “mean square wavenumber conservation” (Liu et al.,) which doesn’t go upscaling. Thus, is “upscale cascade” only a math result?

$$k_M^2 = \frac{\int_0^\infty k^2 E(k) dk}{\int_0^\infty E(k) dk} = \frac{V}{E} = const \quad (4.1.3)$$

- (2) Does straining (vorticity elongation) work along with vortex stretching to accelerate enstrophy cascade and decelerate energy cascade?

Before discussing the physical mechanism of cascade, we shall see the simulation first.

4.2 Model setting

The domain size is set to $[0, 2\pi] \otimes [0, 2\pi]$, with 512^2 grid points, 170^2 Fourier components. No extra smoothing has been added.

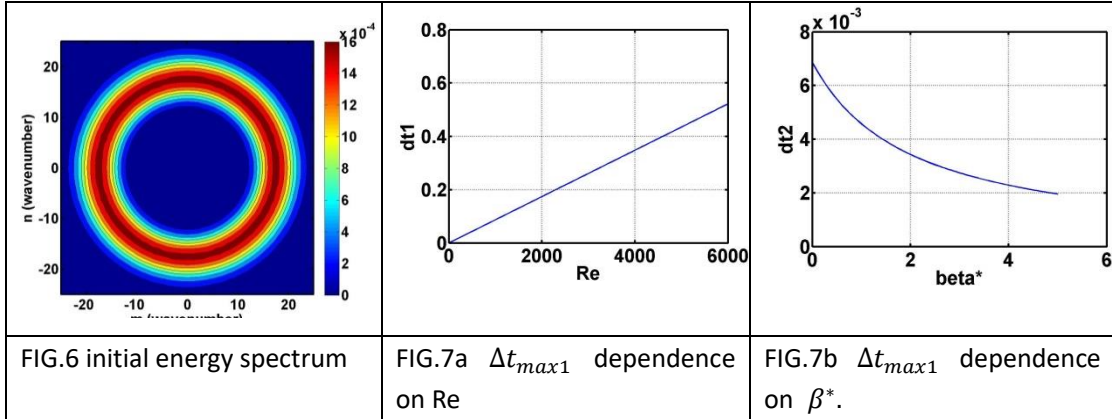
The initial condition is set by prescribing kinetic energy spectrum concentrated around a peak wavenumber k_p (San et al., 2014):

$$E(k) = \frac{a_s}{2} \frac{1}{k_p} \left(\frac{k}{k_p}\right)^{2s+1} \exp\left[-\left(s + \frac{1}{2}\right)\left(\frac{k}{k_p}\right)^2\right] \quad (4.2.1)$$

where $k = \sqrt{m^2 + n^2}$, s is shape parameter --- the larger, the sharper, a_s is used to normalize or adjust the magnitude of $E(k)$. The magnitude spectrum of vorticity is obtained with $|\widetilde{\zeta}_k| = \sqrt{kE(k)}$. The phase part is set with white noise $\xi(m, n)$, $m \in 0, 1, \dots, M$, $n \in -N, \dots, 0, \dots, N$. The $m < 0$ part is set with the conjugate relation: $\xi(m, n) = \xi(-m, -n)$.

$$\widetilde{\zeta}_{m,n} = \sqrt{kE(k)} \exp(i\xi) \quad (4.2.2)$$

I set $k_p = 18$ and $s = 10$ in all simulations. a_s is set to normalize the spatial mean velocity $\overline{u^2 + v^2} = 1$. The initial amplitude spectrum of ψ is shown in FIG.



As for the simulation plan, I work on $Re = 2000, 4000, 6000, 8000$ for $\beta^* = 0$ (called EXP_b0_Re2000, EXP_b0_Re4000, EXP_b0_Re6000, EXP_b0_Re8000), and $\beta^* = 0, 1, 3, 5$ for $Re = 6000$ (called EXP_b0_Re6000, called EXP_b1_Re6000, called EXP_b3_Re6000, called EXP_b5_Re6000).

As for time stepping, the linear stability criterion of R-K 3 scheme is:

$$\Delta t \leq \Delta t_{max} = \min\left(\frac{2.515Re}{M^2}, \frac{2.333}{M(|c|+\beta^*)}\right) = \min(\Delta t_{max1}, \Delta t_{max2}) \quad (4.2.3)$$

I set $|c| = 2$ to represent the dependence of Re on Δt_{max1} and β^* on Δt_{max2} is plotted in FIG. 7a and FIG.7b. Following (San et al., 2014), I choose a very small $\Delta t = 2 \times 10^{-4}$, with a maximum CFL = $\frac{\Delta t}{\Delta t_{max}} \sim 0.1$ for the most stringent $\beta^* = 5$ case, so as to reduce temporal truncation error.

All EXP_b0 (with different Re) experiments run for 10^5 steps, from $t = 0$ to $t = 20$. All EXP_Re6000 (with different β^*) experiments run for 3×10^5 steps, from $t = 0$ to $t = 60$. Each experiment uses 24 cores on Tianhe-2 supercluster, cost about 4 hours (wall clock time) to cover 10^5 steps.

4.3 2D turbulence without beta effect

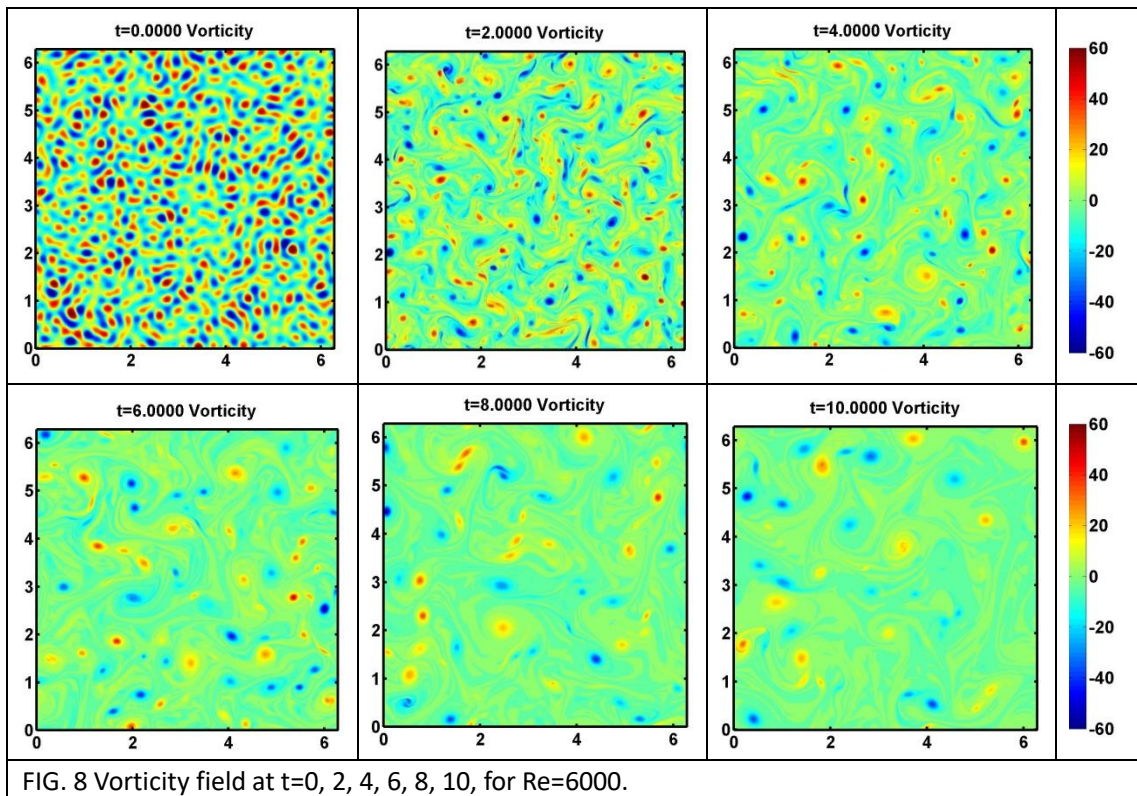
Turbulence without beta effect can be viewed as an asymptotic limit for turbulence on a plane as $Ro \rightarrow 0$, the flow is steered by rotation with Taylor-Proudman theorem.

In all experiments, the flow begins with a dense population of vortices, evolves with vortex merging and crude swallowing, and ends-up with a few strong and large vortices wandering in the open domain. FIG shows the vorticity field at $t=0, 2, 4, 6, 8, 10$ of EXP_beta0_Re6000 run.

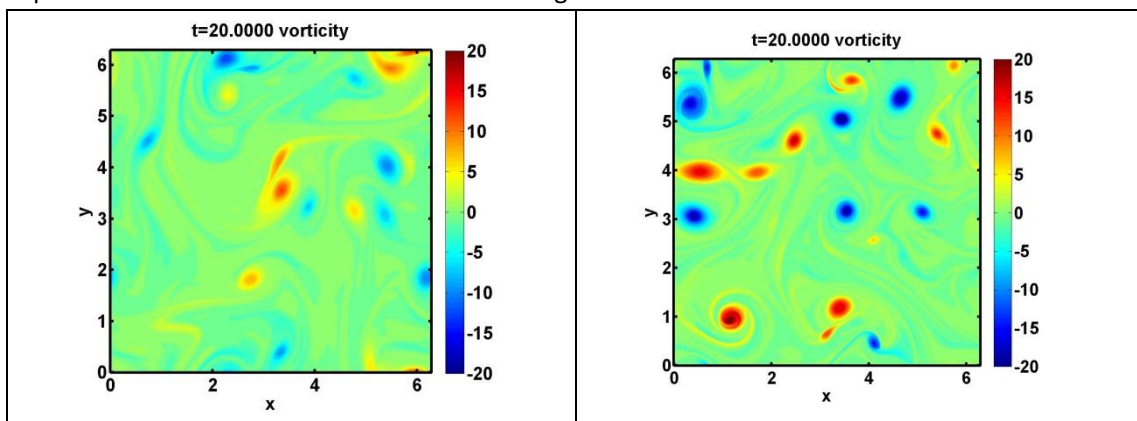
4.3.1 Flow evolution

The flow seems to have undergone two stages. At the first stage, approximately from $t=0$ to 4, neighboring like-sign vortices quickly merge. One vortex imposes straining on the other, forming long thin vortex filaments (vorticity elongation) before they merge. Some filaments break up before merging, and form free-evolving hair-like structures between vortices. At the second stage, approximately later than $t=4$, neighboring vortices have been swept out, and some strong but compact vortices sparsely adorn the flow. They rarely merge due to far distance, and they move and co-rotate with each other more like point vortices. Viscosity continuously smooths the flow, fading the vortices in contour plot, and decelerates vortex motion by reducing vorticity magnitude.

The reason why like-sign vortices merge may be a result of straining. In far field case, one vortex's induced flow looks like parallel flow on the other vortex, which makes it move rather than strain it apart. In near field case, the vortex feels like being stretched apart, forming a vortex filament which transfers vorticity between linking the predator and prey. What's more, the flow topology is different between like-signed and opposite-sign vortices. Like-signed vortices form a saddle point where fluid parcel's trajectory is uncertain to return to the original vortex or enter the other. This enhances the mass exchange between two vortices, just like "mixing". For opposite-sign vortices, there is a jet splitting them apart, which reduces mass exchange just like what westerly jet does for polar vortex in terrestrial atmosphere. Thirdly, viscosity can help fill out the two vortices' interspace, and smear the two vortices into one.



To compare between different Re , The vorticity field at $t=20$ of $Re = 2000, 400, 6000, 8000$ are shown in FIG. This is the last frame of the experiments, with large vortices wandering in the flow. $Re=2000$ case is smoother than other high Re ones due to the excessive viscosity, while other cases are quite similar in magnitude. Such nonlinear trend is also observed in the spectrum comparison between different Re in FIG. In San's paper [], spectrum at $t=2$ is almost insensitive to Re larger than 3000.



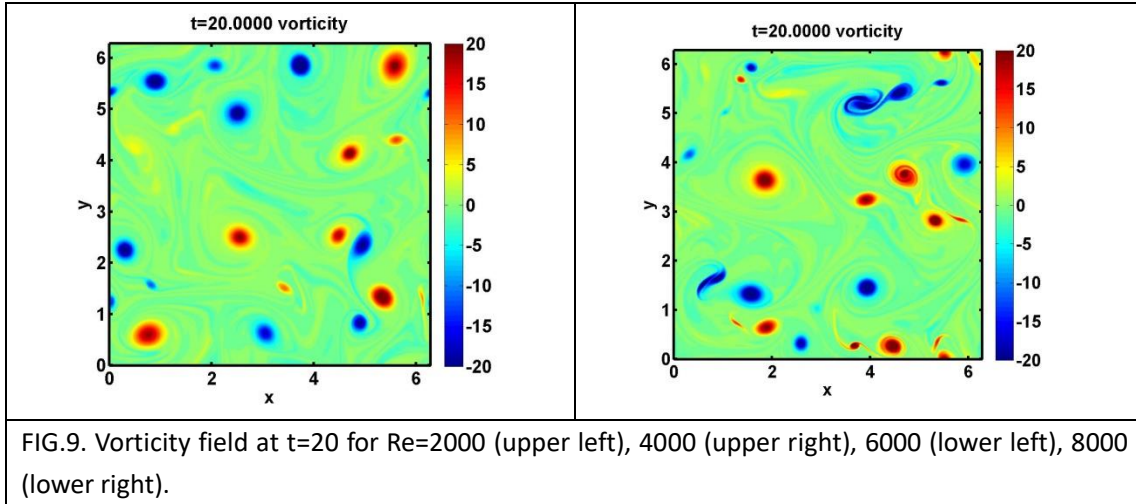


FIG.9. Vorticity field at $t=20$ for $Re=2000$ (upper left), 4000 (upper right), 6000 (lower left), 8000 (lower right).

4.3.3 Energy spectrum

The kinetic energy spectrum $E(k)$ can be estimated with dimensional analysis. Kolmogorov's local hypothesis assumes a temporal equilibrium spectrum $E(k)$, with energy injection rate is far larger than dissipative scale. This leaves a range in wavenumber space that has purely energy transfer (cascade), called "inertial range". The word "locality" means spectrally local --- a specified wave only consumes and feeds the wave right shorter / longer than him. This precludes the transfer of energy directly from a distant wavenumber which may exist in reality. As there is no injection or dissipation in inertial range, the full energy dissipation rate ε balances the full injection rate, equating the energy transfer rate which could serve as a characteristic quantity. ε and k is enough to constitute $E(k)$, but here we use a more intuitive way of using time scale τ_k as an intermediate variable.

From the definition, $\varepsilon \sim \frac{v_k^2}{\tau_k} \sim \frac{kE(k)}{\tau_k}$, and a pure dimensional relation $\tau_k \sim \frac{1}{kv_k} \sim \frac{1}{k\sqrt{kE(k)}}$.

Equating the two formulas by eliminating τ_k , we obtain the energy inertial range spectrum $E(k) \sim \varepsilon^{2/3} k^{-5/3}$. It is observed for scale larger than forcing scale k_f .

We know enstrophy could also cascade, and have a region where locality hypothesis is valid and therefore an enstrophy inertial range. Let's change ε into $\eta \sim \frac{\zeta_k^2}{\tau_k} \sim \frac{k^3 E(k)}{\tau_k}$ (enstrophy dissipation rate), and with $\tau_k \sim \frac{1}{k\sqrt{kE(k)}}$ unchanged, we get enstrophy inertial range $E(k) \sim \eta^{2/3} k^{-3}$ which is at wavenumber far larger than k_f .

FIG shows the the evolution of $E(k)$ for different Re . the 2D spectrum is calculated with:

$$E(k) \approx \sum_{k-1/2}^{k+1/2} (m^2 + n^2) Z_{mn}, \quad k = \sqrt{m^2 + n^2}, \quad m = -M, \dots, 0, \dots, M \quad n = -N, \dots, 0, \dots, N$$

The large picture is similar between all cases. The initial arbitrary spectrum is steep, with a central wavenumber of $k = 18$. Cascade went on swiftly and causing drastic change of $E(k)$ before $t=2$. Then, the shape of the spectrum gradually get steeper, but shifts to smaller wavenumber (red shift) as one. There is energy accumulation ("condensation") at the large wavenumbers, corresponding to the large compact vortices in FIG.def.

The spectrum slope between $10^{0.9}$ to $10^{2.2}$ is close to (but steeper than) k^{-3} , without a $k^{-5/3}$ regime. The large Re , the closer to k^{-3} slope. The Similar shape has also been observed

by the free-decaying simulation of (San et al., 2014). The spectrum even got steeper and farther from k^{-3} with evolution, possibly because large scale vortices began to dominate, but I don't know why. Thus, in free-decaying cases, the spectrum is essentially not temporally steady, and there is no forcing scale k_f . Although there is still energy upscale cascade, there is no energy inertial range, only enstrophy inertial range. What's more, the $E(k)$ scaling law is based on steady hypothesis, but the shift of central wavenumber k_E results from spectrum broadening which only occurs in an unsteady spectrum. Thus, is the scaling law applicable to free-decaying 2D turbulence?

At around $10^{2.45}$ (for all experiments), the spectrum suddenly goes steeper, and this point does not change with time. This is probably the dissipative scale k_v . It is obtained by equating the τ_k in the definition of $\eta \sim \frac{k^3 E(k)}{\tau_k}$, and the scaling counterpart of $J(\psi, \nabla^2 \psi) = \nu \nabla^4 \psi$: $\tau_k \sim \frac{1}{k^2 \nu}$, and finally we get $k_v \sim (\frac{\eta^{1/3}}{\nu})^{1/2}$. As I don't know how to calculate η in a free-decaying 2D turbulence, I haven't theoretically deduced k_v . However, if k_v really doesn't depend on ν (Re) as is suggested in my simulation, then η must not be a constant for different Re.

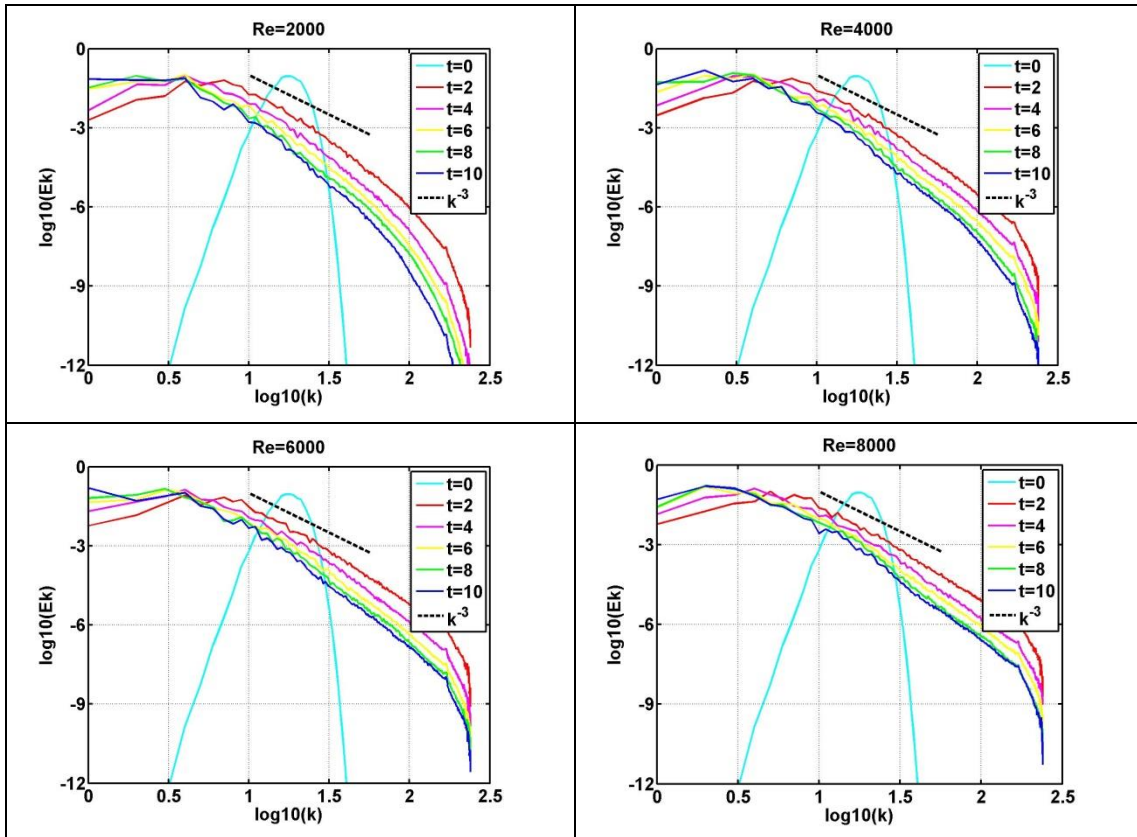


FIG.10. Energy spectrum for Re=2000, 4000, 6000, 8000 cases at different time.

4.3.4 The physical mechanism of cascade

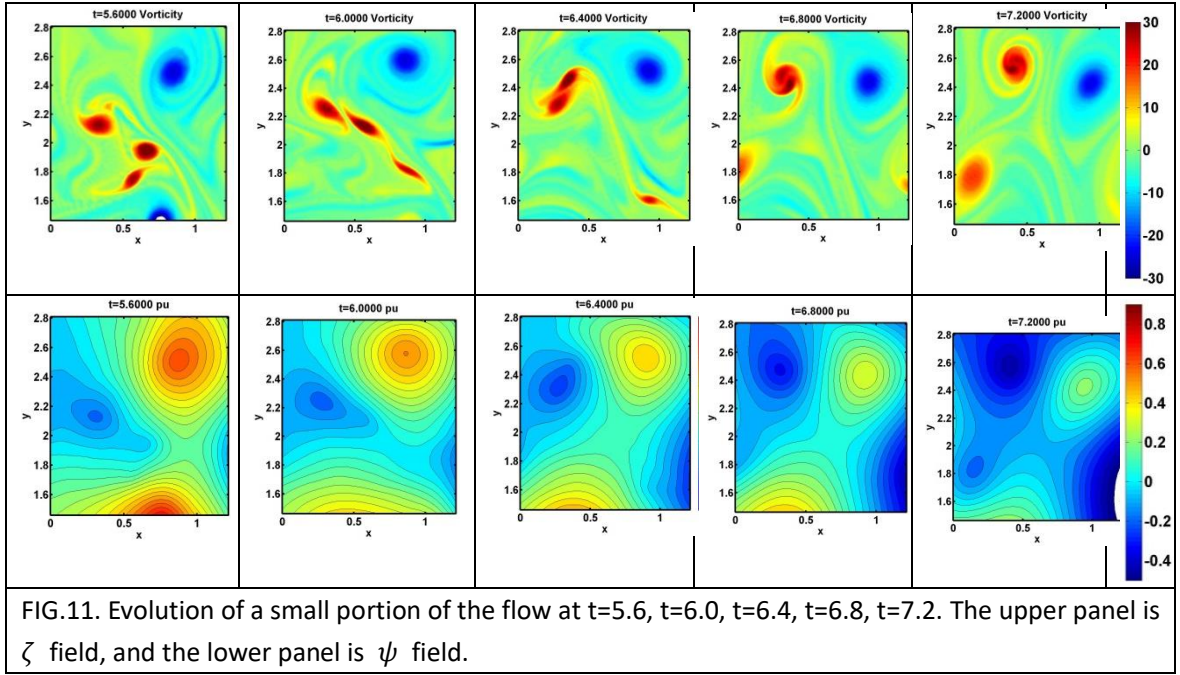
We have witnessed that vortex merge (a kinetic phenomenon) in physical space goes along with energy upscale cascade in spectral space. Vorticity elongation always accompanies vortex merge. I shall introduce Vallis' explanation for cascade based on elongation process, and my understanding based on vortex merge process.

Firstly, Vallis presented an analysis considering only the elongation process. As his description is simple, I shall add some personal understanding. He supposes the larger disparity between small and large vorticity gradient must increase its integral $\int \frac{1}{2} |\nabla \zeta|^2 dS$, and therefore smaller scale enstrophy evolves. As for upscale kinetic energy cascade, he uses Poisson equation $\zeta = \nabla^2 \psi$ to derive a scaling: $\psi \sim \zeta L^2$. With $L_{short} \cdot L_{long} \sim const$, the asymmetrization process broadens the distribution of L , and large L^2 may dominate the vortex size spectrum (if we can define one!). As ζ remains unchanged in an elongated vortice, large ψ will dominate as well (also shown in FIG, and will be revisited later). Because the ψ of a vortex may be expressed as $\approx \int_{-\infty}^r V_{\theta} dr \approx \int_{-\infty}^r \zeta r dr$, larger and stronger vortices may have larger $|\psi|$. Thus, “large ψ dominates” is equivalent to “large vortex dominates”, and therefore kinetic energy upscale cascade.

I would like to add an explanation for kinetic energy downscale cascade. As ψ is a Lagrangian quantity as well, it elongates in a similar way to vorticity. However, it's gradient's integral --- kinetic energy $E = \frac{1}{2} \int |\nabla \psi|^2 dS$, is conserved. Power-conserved ζ leads to power-increasing ζ gradient, so could there be a “power-decreasing” or smoother ψ with power-conserved ψ gradient? If ψ becomes smoother, then we can prove upscale cascade with the above arguments about ψ and vortex size.

Secondly, we may further understand cascade with vortex merge. The vorticity elongation picture is probably not enough to explain the formation of large scale ψ gyres. He said “Because stretching occurs, on average, in all directions, the overall scale of the ψ will increase in all directions...”. Such “in all directions” may be best explained by the circularly entangling of vorticity elongation in a vertical flow, or in other words, the axisymmetrization process of a newly-merged vortex. FIG shows a vortex merge event from $t=5.6$ to $t=7.2$. There are three positive vortices interacting with each other. The lower one was strained into an oval but managed to escape. The middle and upper one formed long filaments before collapsing into each other by $t=6.4$. Then they entangle into one larger vortex and some of the filaments coiled into the vortex while the farther parts was sprayed into free space as the abundance. Those abandoned filaments usually organized into large gyre pattern surrounding those compact vortices. The ψ field is not as colorful as ζ , and the merging events is not apparent from contour topology. The two merging vortices even do not have two clusters of closed contour lines. However, the magnitude of ψ increased during the merging events, in accordance with Vallis' hypothesis that stream function grows larger. A similar case is the geopotential and vertical vorticity field of 500 hPa atmosphere: geopotential field ($\frac{1}{f} \nabla^2 \phi' = \nabla^2 \psi' = \zeta$) is smoother than vorticity, due to the coarsening effects of ∇^2 operator.

In a word, Lagrangian tracers are “stirred” and elongated by the flow, while their topology is unchanged, with contour lines coiling together, forming complex patterns. ψ is not stirred into complex picture, but organizes to larger and more regular patterns in the process.



5. Turbulence and waves on β plane

For geophysical flow on a rotating sphere, if the scale of interest is sufficiently small so that the latitudinal change of Coriolis parameter can be approximated to be linear, then we can introduce the “tangent plane approximation” --- $\beta = df/dy = const.$ For pure 2D flow, there’s no stretching and tilting, so f only appears as df/dy in the vertical vorticity equation. Thus, the domain in y direction can be also periodic in BVE (even in the case partially considering stretching effect with $-\psi/L_d^2$), while not applicable to shallow water equations.

The simulation setting for β plane experiments are the same as $\beta = 0$ cases before, but more time steps up to t=80. There are 4 experiments, with $\beta^* = 0, 1, 3, 5$, with the same $Re=6000$.

For the case $\beta^* \ll 1$, the nonlinear advection term dominates and the flow is similar to the usual 2D turbulence where upscale cascade leads to domain-scale large vortices. For $\beta^* \ll 1$, advection term is omitted and the equation becomes the linear Rossby wave equation and no turbulence exists (assuming inviscid):

$$\frac{\partial}{\partial t} \nabla^2 \psi' + \beta v' = 0 \quad (5.0.1)$$

Substitute normal mode into the linearized equation: $\psi = \psi_0 \exp(-i(k_x x + k_y y - \omega t))$, we get,

$$\omega = -\frac{\beta k_x}{k_x^2 + k_y^2} \quad (5.0.2)$$

The length scale where advection term and β term balances is Rhines scale k_β . By equating Rossby wave frequency to the advection frequency:

$$|U k_\beta| = \left| -\frac{\beta k_x}{k_x^2 + k_y^2} \right| = \frac{\beta k_\beta |\cos\theta|}{k_\beta^2} \quad (5.0.3)$$

We get $k_\beta^2 = \frac{\beta}{U} |\cos\theta|$, where θ is the phase angle in wavenumber space. The k_β has a dumbbell like contour line. As there is energy upscale cascade in 2D turbulence, small scale disturbance will reach k_β . For $k > k_\beta$, nonlinear effect is suppressed and upscale cascade may halt, causing energy accumulation around k_β . Thus, the cascade of turbulence on β plane is anisotropic, with a zonal preference. For $k \sim k_\beta$, Rossby wave and turbulence co-exist, and their interaction can induce zonal jets in forcing-dissipation cases.

5.1 Transition to waves shown in Hovmoller diagram

Hovmoller diagram is a t-x contour plot particularly useful in wave or coherent structure detection. In other words, the contour lines are parallel to the characteristic line. Thus, following (Rhines, 1975), we plot this diagram.

Let's begin with $\beta^* = 5$ case. The Hovmoller diagram of ψ (sampling the cross-section of $x=0$) from $t=20$, show the transition from turbulence to waves. Band-like structure in Hovmoller diagram appears by $t=2.5$. The minus skew of stream function iso-surface line (wave front) indicates westerly travelling wave with a phase speed about 1.26. There is intermittency by $t=15$ and $t=25$ (why?), but general trend is that structures became more organized, with larger stream function (denoting larger structures). The wave front became smoother by $t=30$, showing a faster westerly phase speed, probably because longer waves (caused by upscale cascade) travel faster. For the control run $\beta^* = 0$, there's no Rossby wave and no band-like structures existed. With increasing β^* , Rossby wave moves faster in general due to larger β^* in (5.0.2), but there is no apparent differences between $\beta^* = 1$ and $\beta^* = 3$.

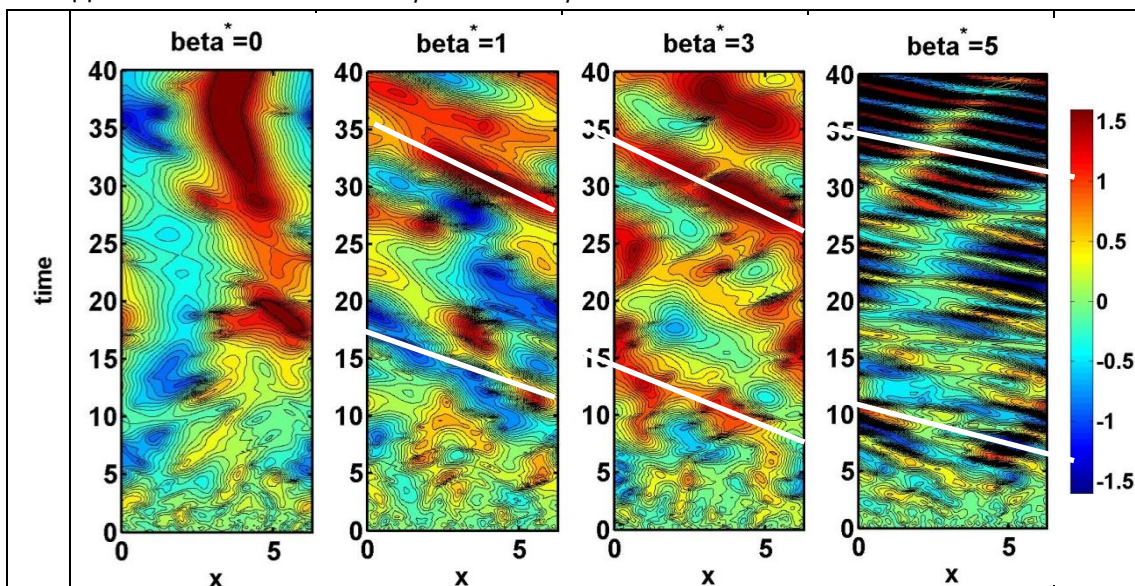


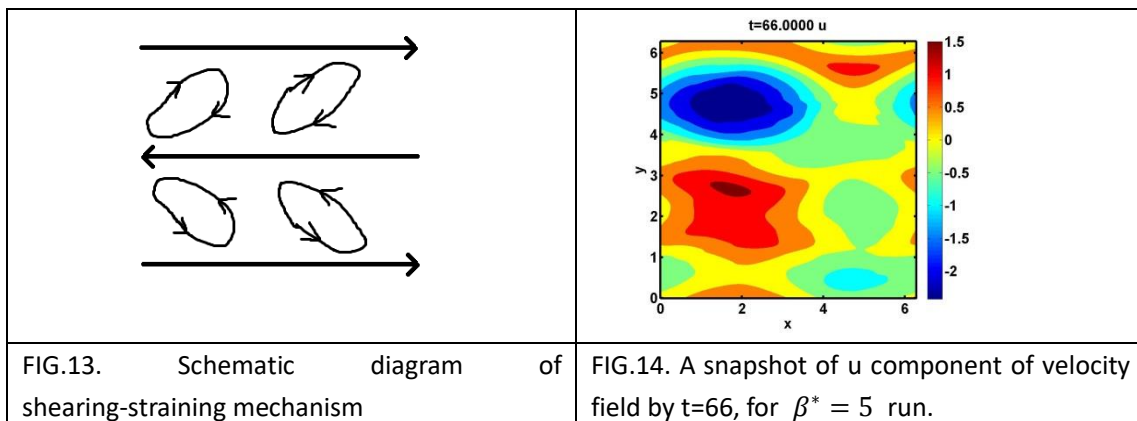
FIG.12. Hovmoller diagram for stream function's cross-section at $x = 0$. The left most panel is the control run.

5.2 Coherent structure evolution

To see the evolution of coherent structures and further divide the regime, we look at the $\beta^* = 5$ vorticity field and see that the flow has three stages.

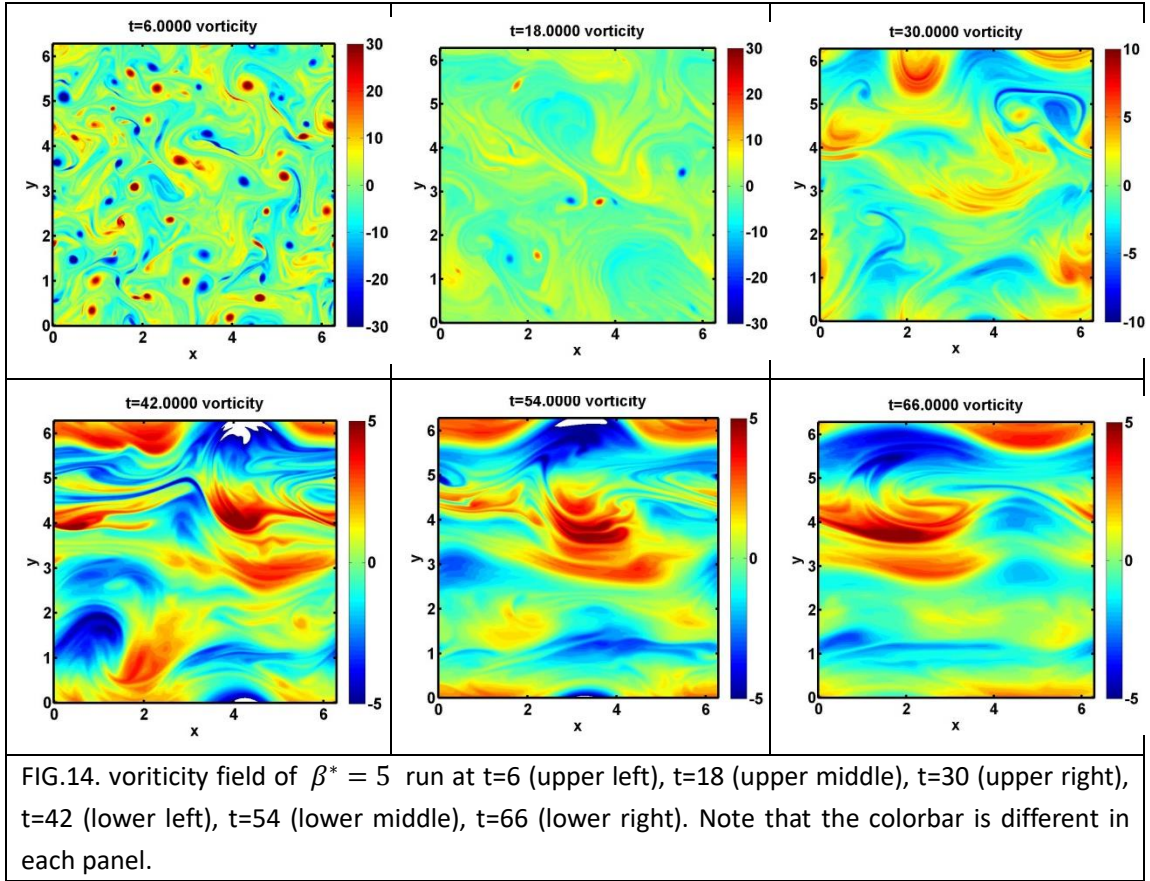
At the first stage, from $t=0$ to $t \sim 6$, vortices evolve similar to the f-plane case, with small vortices merge with their neighbours.

At the second stage, from $t \sim 6$ to $t \sim 20$, vortices are no longer that crowded and vortex motion dominates vortex merge events. The vortex filaments which failed to coil into the new vortex, did not behave silently as they did in f-plane case. They organized into large patches which stuck some vortices onto it and carry them moving, as if insects got caught on a spider net) which carried the vortices rotating or shifting. Vortex merge events became very rare, because vortices were carried by the large structure and shifted together, losing their freedom of “falling in love”. As a result, vortices began to decrease in size after reaching their largest stage, probably because of diffusion. Meanwhile, as the large structure has a strong straining, vortices were elongated into long thin filaments (not by other vortices as is the case for f-plane run). They were finally absorbed by the large structure and contribute to its strength. Similar process has occurred in jovian atmosphere and formed the basis for “shearing-straining” mechanism (Vasavada et al., 2005) of jet formation. For example, in a $\partial \bar{u} / \partial y > 0$ (anti-cyclonic shearing) base flow, the anti-cyclonic eddies are tilted into northeast-southwest direction. The northward branch of the eddy have positive u' , and the southward branch has negative u' , leading to $\overline{u'v'} > 0$. Thus, we have $\overline{u'v'} \partial \bar{u} / \partial y > 0$, an upgradient transport of zonal momentum by anti-cyclonic eddies acts to accelerate the base flow. For cyclonic eddies, however, we have $\overline{u'v'} \partial \bar{u} / \partial y < 0$, and have decelerating effect (Vasavade et al., 2005).



What’s more, I haven’t seen Rossby wave emission by vortices as I once expected, why?

At the third stage, that is later than $t \sim 20$, most vortices had broken into filaments: not by straining from other vortices, but probably by Rossby wave dispersion (by themselves) (McWilliams et al., 1979). “Shell-like” Rossby wave structures began to dominate the field. For a cyclonic region, the vorticity patches are smooth on its north side and coarse on the south side (like fingers), but for an anti-cyclonic region, vice versa. Take $t=66$ for example, we see at the upper most part of the domain, there is a meandering easterly jet shown in the velocity field (right panel of FIG.12). The jet is between a pair of positive and negative vorticity bands, with sharp contour lines. Thus, the sharp region of “shell” patches may be caused by the strong shearing of jet. For the coarse region, I haven’t got an answer.



5.3 End states: jets vs. vortices

For $\beta^* = 5$ run, the end state is jet and Rossby wave as shown in FIG.14 and FIG.15 and FIG.16. There are 3 prograde (eastward) jets and 2 retrograde (westward) jets. The knots in FIG.16 are wave ridges and crests, and manifested that the jets are meandering. Let's check whether the jet's nondimensional distance scales as nondimensional L_β^* . Set $U \sim 0.8$, $\beta^* = 5$, we get:

$$L_\beta^* = 2\pi \sqrt{\frac{U}{\beta^*}} \sim \frac{2\pi}{2.5} \quad (5.3.1)$$

The Rhines scale predicts 2.5 pairs of jet, which agrees with our experiment. Further tests of scaling is required. What's more, the magnitude of vorticity doesn't dissipate much after t=42, which is also the case for the f-plane run. This is probably because viscosity is most effective in small scale.

For $\beta^* = 0$ control run, vortices just merged and grew, remaining a few large vortices and they moved around each other silently but aggressively, waiting for the right moment of attacking. For the later moments of simulation, there were no steady zonal structures shown in the right panel of FIG.15. At t=66, there are 2 cyclones and 4 anti-cyclones as are shown in FIG.14. Vortex motion still occurs, even though rare.

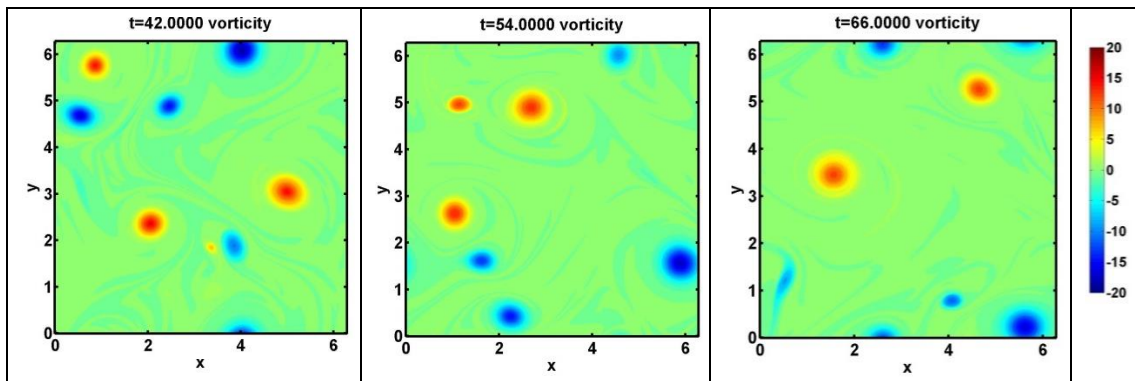


FIG.15. vorticity field but for $\beta^* = 0$ control run at t=42 (lower left), t=54 (lower middle), t=66 (lower right).

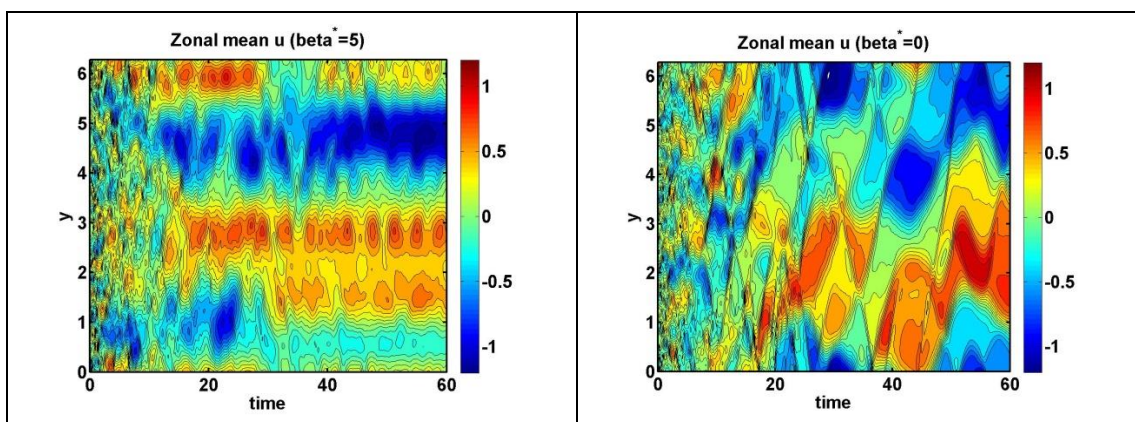


FIG.16. zonal mean zonal wind's evolution with time. The left panel is $\beta^* = 5$ run (with clear jet structure), and the right panel is $\beta^* = 0$ (f-plane) control run.

6. Conclusion

Through this numerical investigation of 2D turbulence in barotropic vorticity equation, I have reviewed the knowledge I learnt in GFD course, books and papers. The beautiful structure of turbulence is impressive, and the rich phenomenon of 2D turbulence almost contains half of the GFD theory. There is a few questions I haven't been able to answer:

- (1) For free-decaying f-plane turbulence, can we define an equilibrium spectrum? Why can't we see $k^{-5/3}$ regime in a free decaying case ?
- (2) For f-plane 2D turbulence, is the number of freedom decreasing with time evolution ? --- the end state may be depicted with point vortex dynamics.
- (3) For f-plane 2D turbulence, are "mean square wavenumber conservation" and "energy upscale cascade" two conflicting concepts?
- (4) For beta-plane 2D turbulence, the transition from turbulence to Rossby wave is clear in Hovmoller diagram, and maybe on spectrum as well, but what's the physical mechanism? Is it straining of vortices by large scale structure (without much change in topology), or the wave dispersion of vortex itself ?
- (5) What if we add forcing?
- (6) What's the vortex profile of 2D turbulence? Do they suffer from any hydrodynamic instability?

- (7) What's the dynamics of vortex filaments, which have been discarded into the free space?
It seems that they are important for beta-plane turbulence.
There are a lot of questions that are not shown here, and they are left for future.

7. Acknowledgement

I thank Prof. Jianhua Lu for teaching the fantastic GFD course. I thank Prof. A.P. Showman and Prof. Yongyun Hu for introducing me the field of planetary atmosphere. I thank my advisor Prof. Yihua Lin for helpful discussion and computational funding. I thank Tianhe-2 cluster in National Supercomputing Center in Guangzhou for the computational resource.

References

- [1] Vallis, Geoffrey K. *Atmospheric and ocean fluid dynamics: Fundamentals and large-scale circulation*. 2006.
- [2] McWilliams, James C. *Fundamentals of Geophysical Fluid Dynamics. Fundamentals of geophysical fluid dynamics*. Cambridge University Press, 2006.
- [3] Durran, Dale R. *Numerical Methods for Fluid Dynamics With Applications to Geophysics. Numerical methods for fluid dynamics /*. Academic Press, 2010
- [4] Vasavada, Ashwin R, and A. P. Showman. "Jovian atmospheric dynamics." *Reports on Progress in Physics* 8(2005):1935-1996.
- [5] McWilliams, J. C, and G. R. Flierl. "On the evolution of isolated, nonlinear vortices." *Journal of Physical Oceanography* 9.6(1979):1155-1182.
- [6] Boffetta, Guido, and R. E. Ecke. "Two-Dimensional Turbulence." *Annual Review of Fluid Mechanics* 44.3(2011):427-451.
- [7] San, Omer, and A. E. Staples. "High-order methods for decaying two-dimensional homogeneous isotropic turbulence." *Computers & Fluids* 63.63(2012):105–127.
- [8] Rhines, P. B. "Waves and turbulence on a beta-plane." *Journal of Fluid Mechanics* 69.3(1975):417-443.
- [9] Taylor, John R. "Numerical simulations of the stratified oceanic bottom boundary layer." *Dissertations & Theses - Gradworks* (2008).
- [9] 《快速傅里叶变换：算法与应用》 [美] K.R.Rao, D.N.Kim, [韩] J.J.Hwang, 万帅, 杨付正译, 机械工业出版社： 2016.
- [10] 《数值模式中的谱方法》，雷兆崇，章基嘉编著，气象出版社： 1991.
- [11] 《大气动力学》（上、下册），刘适式、刘适达编著，北京大学出版社： 2009.

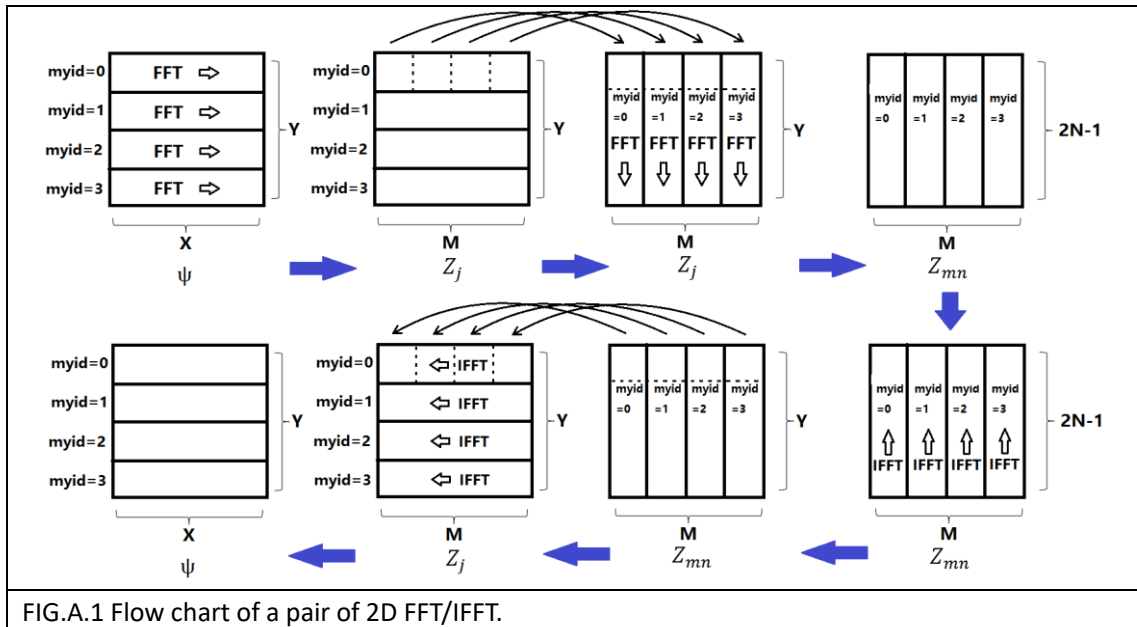
Appendix. A Parallel Computation Scheme

The code is MPI-parallelized to save computation time. The initial condition is set by root process, and then the data are sent to other processes. All computing processes (spectral transform, grid point multiplication, etc.) are distributed. When we need an output, the data is sent to the root process and a netcdf-format file is written.

The parallel computation scheme is similar to the DIABLO model introduced in Dr. John Taylor's PhD thesis (Taylor, 2008). The method of FFT is adopted from a FFT introductory book (Rao et al., 2016).

As all multi-dimensional transforms are split into a series of 1D transform, data is set to be continuous for each transform call. The flow chart of a 2D FFT and a 2D IFFT shown in FIG.A.1.

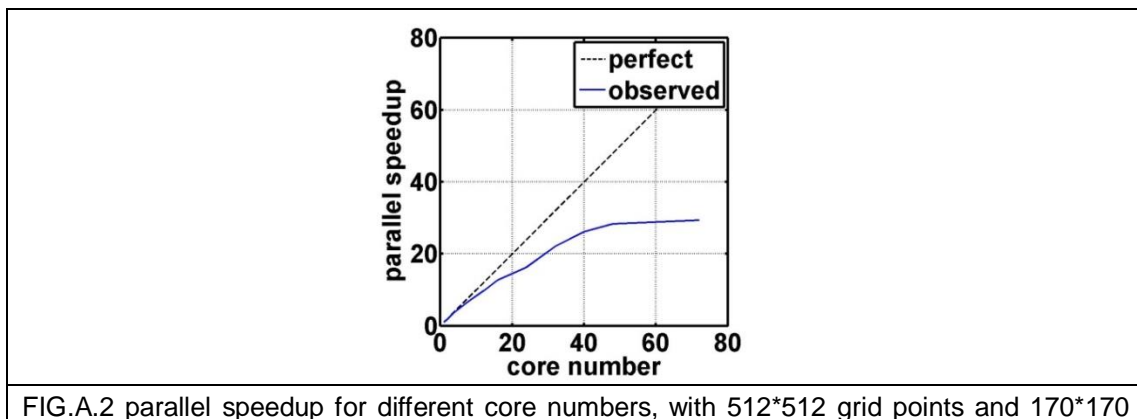
Suppose we have n cores. Before FFT in x-component, all data are zonally distributed, with a size of $X*(Y/n)$ for each process. After a FFT operation, the size of each array becomes $M*(Y/n)$. To prepare for the FFT in y direction, the arrays are transposed with a loop communication MPI call, and the size of each array is $(M/n)*Y$. After the FFT call in y direction, the size becomes $(M/n)*(2N-1)$. Here, $2N-1$ denotes wavenumbers from $-(N-1), \dots, 0, \dots, N-1$. The inverse transform is similar.



The parallel speedup is introduced to evaluate the parallel efficiency, and a speedup test result is plotted in FIG.A.2. The term is defined as:

$$\text{parallel_speedup}(n) = \frac{\text{wall_clock_time}(1 \text{ core})}{\text{wall_clock_time}(n \text{ cores})}$$

For an ideal machine with no communication and MPI initialization expense, $\text{parallel_speedup}=1$, which is shown as the dashed line in FIG.A.2. A test with $512*512$ points, $170*170$ waves (the same as the simulation setting in 2D turbulence test) is shown as the solid blue line. The speed of parallel computing increases steadily with increasing core numbers, but the efficiency decays swiftly by $n=40$ cores where communication expense becomes comparable with the time saving by parallel computing.



waves.